The effect of the Coulomb potential on subcycle interference of electron wave packets in atomic ionization by two-colour laser pulses

The effect of the Coulomb potential on subcycle interference of electron wave packets in atomic ionization by two-colour laser pulses

Diego G Arbó

Institute for Astronomy and Space Physics, IAFE (CONICET-UBA), CC 67,
Suc. 28 (1428) Buenos Aires, Argentina

E-mail: diego@iafe.uba.ar

Abstract

We analyse the effect of the long-range potential of the ionic core on the photoelectron emission in atomic ionization by a linearly polarized subcycle sculpted laser pulse of two-colour components, where one frequency doubles the other. The total ionization yield consists mostly of direct electrons, which can be characterized by both *intracycle* and *intercycle* interferences. Using a semiclassical model based on the Simple Man's Model, we can derive an analytical expression for the intracycle interference due to the coherent superposition of different electron trajectories released in the same sculpted optical cycle. In turn, the intercycle interference is the consequence of the superposition of multiple trajectories released at different cycles and is accounted for by the energy conservation in the photon absorption process. We show that a semiclassical description in terms of a diffraction process at a time grating for two-colour laser pulses remains qualitatively unchanged beyond the strong field approximation. In particular, the Coulomb potential shifts the intracycle interference modulations towards the threshold, whereas the intercycle interference pattern remains invariant. The present study completes a recent work by Xie *et al* (2013 *New J. Phys.* **15** 043050), where the influence of the Coulomb field on atomic ionization by sculpted two-colour laser fields is probed but in which path interferences are not considered. Furthermore, this article gives theoretical support to recent experiments with He and Ar where the sub-cycle interference structures originating from trajectories launched within a time interval of less than one femtosecond were observed (Xie X *et al* 2012 *Phys. Rev. Lett.* **108** 193004).

Keywords: Coulomb potential, subcycle interference, two-colour laser, intracycle diffraction

(Some figures may appear in colour only in the online journal)

1. Introduction

In above-threshold atomic ionization by intense laser pulses, electrons are emitted via tunnelling through the potential barrier conformed by the combination of the atomic potential and the external strong field. Photoionization is a highly nonlinear quantum–mechanical phenomenon in which tunnelling occurs predominantly around the maxima of the absolute value of the electric field within each optical cycle. After detachment from the atom, electrons interact with both the laser field and the residual core potential. Photoelectrons can be classified into *direct* and *rescattered* electrons according to the three-step model [3]. Many advances in theory have been attained by neglecting the potential of the ionic core, which results in the strong field approximation (SFA). However, accurate results should involve the effect of the atomic potential on the emitted electron yield.

It has been previously shown that classical trajectories of direct electrons are crucial in the formation of interference patterns in photoelectron spectra for one-colour lasers when the phase of these classical trajectories are considered [4]. In few-cycle pulses, temporal double-slit interference patterns were experimentally measured [5, 6] and theoretically studied [7]. The observation of diffraction fringes in photoionization of He atoms [6] and photodetachment of F$^-$ ions by femtosecond pulses for fixed frequency [8] was theoretically analysed under the SFA [9]. The interference pattern in multi-cycle photoelectron spectra can be identified as a diffraction pattern at a time grating composed of *intracycle* and *intercycle* interferences [4, 9–11]. While the latter gives rise to the well-known above-threshold ionization (ATI) peaks, the former leads to a modulation of the ATI spectrum offering information on sub-cycle ionization dynamics. This analysis was based on a semiclassical model closely following the 'Simple Man's Model' (SMM) for one-colour laser fields [4] and extended to two-colour lasers in [12].

Two-colour pulses with commensurate frequencies, usually consisting of a fundamental component and one of its low harmonics, were used in previous investigations of ATI [13–15], control ionization [16], dichroism [17, 18] and orientation of molecules [19]. Two-colour fields have also been used to sculpt the laser field shape and to control interference fringes in electron momentum emission [2, 12]. Coherent phase control consists of investigating the physical processes involved in atomic ionization as a function of the relative phase φ of the two frequency components of the field [13].

The goal of this paper is to elucidate the action of the atomic core potential on the ionization yield. We analyse the validity of the factorization of the electron emission distribution in terms of a time grating in the presence of long-range Coulomb forces. In the present paper, we generalize this result to atomic ionization by two-colour lasers emphasizing the role of φ in the visibility of intracycle interference pattern. In order to do that, we inspect how the Coulomb potential affects both the intra- and intercycle interference stemming from the superposition of wavepackets released at different emission times. Direct photoelectrons dominate the total ionization yield, therefore, we have omitted rescattering processes in our analysis. We demonstrate that the semiclassical analysis based on the SMM performed for two-colour fields in terms of a time grating [12] remains valid when the Coulomb potential of the atomic core is considered. Furthermore, we present a systematic study of how the intracycle and intercycle interferences depend on the strength of the Coulomb potential. We test the effect of the Coulomb potential by comparing the SMM and the time-dependent distorted wave SFA—both disregard it—with the Coulomb–Volkov approximation (CVA) and the numerical solution of the time dependent Schrödinger equation (TDSE) without approximations—both consider it.

The present article is organized as follows. In section 2, we summarize the calculation methods used: (i) the time-dependent SFA, (ii) a variant of (i) which considers the action of the atomic potential in the final channel called distorted-wave CVA and, at last, (iii) the semiclassical approximation based on the SMM [12]. In section 3, we show and discuss the results of the photoelectron spectra, doubly differential momentum distributions and longitudinal momentum distributions. We conclude in section 4. Atomic units are used along the paper.

2. Review of calculation methods

We consider an atom in the single-active electron approximation subject to a linearly polarized strong laser pulse. The theory is presented quite generally and will be applied later for the special case of a two-colour laser pulse.

The evolution of the electronic quantum state $|\psi(t)\rangle$ is governed by the time-dependent Schrödinger equation

$$i\frac{d|\psi(t)\rangle}{dt} = H|\psi(t)\rangle \tag{1}$$

for the Hamiltonian $H = \vec{p}^2/2 + V(r) + z F(t)$, written in the length gauge, where $V(r)$ is the central atomic core potential, $\vec{p}$ is the momentum of the electron, and $\vec{r}$ the position of the electron. As a result of the interaction, one electron initially bound to the target core in the initial state $|\phi_i\rangle$ with energy $-I_p$, where I_p is the ionization potential, is emitted after conclusion of the pulse into the final unperturbed state $|\phi_f\rangle$ with final momentum $\vec{k}$ and energy $E = k^2/2$, where $k = |\vec{k}|$.

Electron momentum distributions can be calculated from the transition matrix as

$$\frac{dP}{d\vec{k}} = |T_{if}|^2, \tag{2}$$

where T_{if} is the T-matrix element corresponding to the transition $\phi_i \rightarrow \phi_f$. Because the atomic potential is central, the process possesses cylindrical symmetry around the polarization axis and the azimuthal angle is cyclic.

In the rest of the section, we outline the main points of the calculation methods used to determine the electron dynamics in a photoionization process. T_{if} will be computed (i) exactly by solving numerically the TDSE, (ii) within the time-dependent distorted-wave CVA, (iii) its strong field variant (SFA), and (iv) a semiclassical simplification of the latter based on the SMM.

2.1. Time-dependent strong-field approximation (SFA)

The SFA has been developed long time ago to assess atomic photoionization. The well-known Keldysh–Faisal–Reiss (KFR) theory of intense-field processes was developed based on the SFA [20–22] despite further modifications taking account of the important residual Coulomb interaction in the presence of the field [23]. Alternatively, SFA can be derived within the time-dependent distorted wave theory [24], where the transition amplitude in the *post* form is expressed as

$$T_{if} = -i \int_{-\infty}^{+\infty} dt \, \langle \chi_f^-(t) | z F(t) | \phi_i(t) \rangle, \tag{3}$$

and $\chi_f^-(t)$ is the final distorted-wave function. In the present case, the initial state fulfills the Schrödinger equation with the unperturbed atomic Hamiltonian $H_0 = \frac{\vec{p}^2}{2} + V(r)$, with eigenenergy $-I_p$.

Different distorted-wave approximations result from different choices of the distortion potential to be included in $|\chi_f^-\rangle$ [25]. One of the most renowned choices of $|\chi_f^-\rangle$ is the solution of the Hamiltonian $H_f = \frac{\vec{p}^2}{2} + z F(t)$, corresponding to a free electron in the time-dependent electric field (exit-channel distorted Hamiltonian), with eigenenergy $k^2/2$. The mentioned solutions are the Volkov states [26]

$$\chi_{\vec{k}}^{(V)-}(\vec{r}, t) = \frac{\exp[i(\vec{k} + \vec{A}) \cdot \vec{r}]}{(2\pi)^{3/2}}$$
$$\times \exp\left[-i \int_t^{+\infty} dt' \frac{(\vec{k} + \vec{A}(t'))^2}{2}\right], \quad (4)$$

where the exponent in equation (4) is the Volkov action and $\vec{A}(t) = -\int_{-\infty}^t dt' \vec{F}(t')$ is the vector potential of the field multiplied by the speed of light. The inclusion of equation (4) into equation (3) leads to the well-known plane-wave SFA. Accordingly, the influence of the atomic core potential on the continuum state is neglected and, therefore, the momentum distribution is a constant of motion after conclusion of the laser pulse.

For a symmetric electric field, i.e., $F(t) = F(\tau - t)$, it is easy to derive that the final momentum distribution is an even function in the longitudinal momentum [25],

$$\frac{dP(k_z)}{d\vec{k}} = \frac{dP(-k_z)}{d\vec{k}}, \quad (5)$$

where we have assumed that the initial state has even parity, i.e., $\phi_i(\vec{r}) = \phi_i(-\vec{r})$. It is well known that the SFA fails to describe ionization for moderately weak fields as well as the slow electron yield even for strong fields [25, 27]. For this reason, a theory which involves the effect of the atomic potential on the receding electron is considered next.

2.2. Time-dependent distorted-wave Coulomb–Volkov approximation (CVA)

An improved approximation is achieved by combining the atomic eigenstate of the continuum $\phi_{\vec{k}}^-$ with the final-channel wave function of equation (4). For a hydrogenic atom, i.e., $V(r) = -Z_T/r$ with Z_T as the nucleus charge, it results in the Coulomb–Volkov final state firstly proposed by Jain and Tzoar [28] and later extensively used for ionization by monochromatic low-intensity lasers [21, 22, 29, 30, 31, 32]

$$\chi_{\vec{k}}^{(CV)-}(\vec{r}, t) = \chi_{\vec{k}}^{(V)-}(\vec{r}, t) \mathcal{D}_C(Z_T, \vec{k}, \vec{r}), \quad (6)$$

where

$$\mathcal{D}_C(Z_T, \vec{k}, \vec{r}) = N_T^-(k) \, {}_1F_1(-iZ_T/k, 1, -ikr - i\vec{k} \cdot \vec{r}).$$

The Coulomb normalization factor $N_T^-(k) = \exp(\pi Z_T/2k)\Gamma(1 + iZ_T/k)$ coincides with the value of the Coulomb wave function at the origin, and ${}_1F_1$ denotes the confluent hypergeometric function. Inserting equation (6) into equation (3) leads to the CVA, which can be evaluated in closed form [33, 34]. In the CVA, the simultaneous interactions of the released electron with the residual ionic core and the external field are considered non-perturbatively, although only approximately. The forward–backward symmetry of equation (5) is inherent to the SFA (and SMM) but is broken in the CVA because of the inclusion

of the Coulomb distortion in the exit channel [1, 25]. From equation (6), the SFA can be derived as the limit of weak Coulomb potential, i.e., $\chi_{\vec{k}}^{(CV)-} \to \chi_{\vec{k}}^{(V)-}$ as $Z_T \to 0$.

2.3. Semiclassical model

The semiclassical theory closely follows the SMM [3, 35–37] to deal with interference signatures within the SFA. The general outline of the SMM previously introduced for monochromatic electric fields [4, 10, 11] can be applied to the particular case of the two-colour field [12]. The SMM is based on the saddle-point approximation of the continuum distorted wave SFA (equation (3)), which leads to a transition amplitude to the continuum state of the form [36]

$$T_{if}(\vec{k}) = -\sum_{i=1}^M G(t_r^{(i)}, \vec{k}) \, e^{iS(t_r^{(i)})}. \quad (7)$$

Here, M is the number of electron trajectories born at ionization times $t_r^{(i)}$ which reach a given final momentum $\vec{k}$, and $G(t_r^{(i)}, \vec{k})$ is the ionization amplitude,

$$G(t_r^{(i)}, \vec{k}) = \left[\frac{2\pi i F(t_r^{(i)})}{|\vec{k} + \vec{A}(t_r^{(i)})|}\right]^{1/2} d^*(\vec{k} + \vec{A}(t_r^{(i)})), \quad (8)$$

where $d^*(\vec{v})$ is the dipole element of the bound-continuum transition. In equation (7), S is given by the Volkov action of equation (4) [26], where the time dependence of the initial state, i.e., $\exp(-iI_p t)$ is included.

The release time $t_r^{(i)}$ of trajectory i is determined by the saddle-point equation [38],

$$\left.\frac{\partial S(t)}{\partial t}\right|_{t=t_r^{(i)}} = \frac{[\vec{k} + \vec{A}(t_r^{(i)})]^2}{2} + I_p = 0. \quad (9)$$

Release times $t_r^{(i)}$ are complex not only because $I_p > 0$, but also because of the presence of a component of the momentum in the transversal direction. For the sake of simplicity, we approximate the ionization times by real values by setting $I_p = 0$ and $k_\rho = 0$ within the SMM, arriving at

$$k_z + A(t_r^{(i)}) = 0. \quad (10)$$

Classical trajectories originating at different release times $t_r^{(i)}(i = 1, 2, ...)$ can give rise to semiclassical interferences provided they satisfy the condition given by equation (10) for reaching the same final momentum $\vec{k}$.

From this point, we apply the SMM of equation (7) together with equation (10) to the interaction of a target atom with a two-colour laser pulse, where one frequency doubles the other ($\omega - 2\omega$). The pulse is described through the time-dependent electric field $\vec{F}(t)$ along the $\hat{z}$ direction, which reads

$$\vec{F}(t) = f(t)[\cos(\omega t) + \cos(2\omega t + \varphi)]\hat{z}, \quad (11)$$

where ω is the fundamental laser frequency, φ the relative phase between the two frequency components and $f(t)$ is the envelope function of the sculpted laser pulse. By varying the relative phase φ, the ionizing field (figure 1), emission times and the motion of the interfering wave packets can be controlled on an attosecond time scale. In figure 1(a), for laser fields with relative phase $\varphi = 0$, two solutions per optical cycles are observed: the early and late release times marked
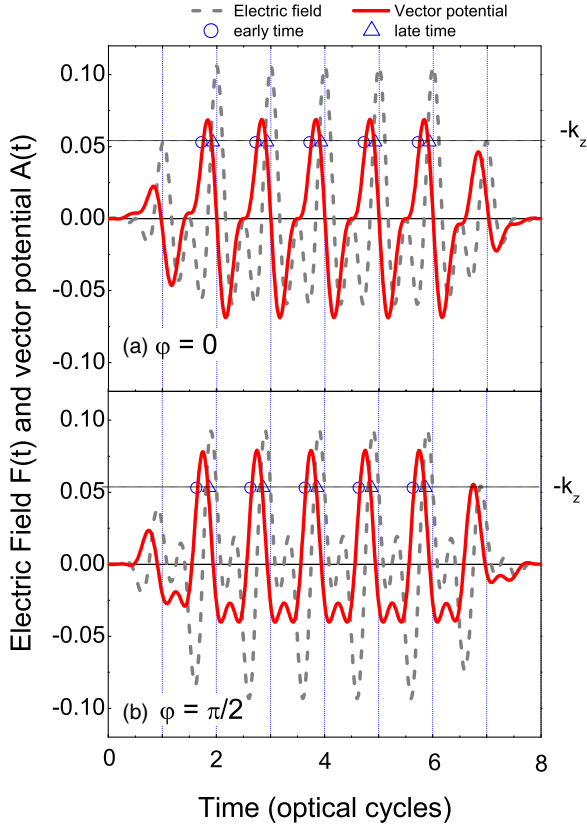
Figure 1. Electric field in dashed line and vector potential (solid line) of a sculpted $\omega - 2\omega$ laser pulse as a function of time for relative two-colour relative phases $\varphi = 0$ (a) and $\varphi = \pi/2$ (b). Circles represent early ionization times and triangles late ionization times within the SMM. The amplitude field is $F_0 = 0.0533$ (corresponding to $I = 10^{14}$ W cm^{-2} for a one-colour pulse). The frequency is $\omega = 0.057$ (800 nm). The pulse duration is eight optical cycles ($\tau = 21$ fs) with a two-cycle ramp on, two-cycle ramp off and four-cycle flat top central region (see equations (11) and (17) in text). The vector potential is multiplied by the frequency ω for a better visualization.

with circles and triangles, respectively. Within the SMM, we consider a flat top pulse, i.e., $f(t) = F_0$ in the main region of the pulse consisting of N optical cycles, and neglect the ionization probability during the adiabatic switch on and off.

For an electric field of equation (11) with relative phase $\varphi = 0$, the momentum distribution along the polarization axis is symmetric (equation (5)) within the SMM and SFA. According to figure 1(a), the classical range is $-k_z|_{\max} < k_z < k_z|_{\max} = (3\sqrt{3}/2)F_0/\omega$. The maximum classical kinetic energy can be directly derived from $E_{\mathrm{cl}} = (k_z|_{\max})^2/2 = 2.7U_p = 2.7(5/4)F_0^2/4\omega^2$. The forward–backward symmetry of equation (5) is broken within the SFA for relative phases different from zero (or multiples of π), for which $\vec{F}(t) \neq \vec{F}(\tau - t)$. From figure 1(b) for the case of $\varphi = \pi/2$, the final electron longitudinal momentum covers a range $k_{\min} < k_z < k_{\max}$, where $k_{\min} = -(3/2)F_0/\omega$ doubles (in absolute value) $k_{\max} = (3/4)F_0/\omega$. This results in a very asymmetric distribution with maximum kinetic energy $k_{\min}^2/2 = (9/8)F_0^2/\omega^2$ in the backward direction, which is four times the maximum energy $k_{\max}^2/2 = (9/32)F_0^2/\omega^2$ in the forward direction. Therefore, the maximum drift energy

results to be $(9/2)(F_0^2/4\omega^2) = (18/5)U_p$, which means that we have gained 80% with respect to the well-known one-colour maximum classical kinetic energy $2U_p$.

For the sake of simplicity, in the rest of this section, we neglect the contribution of more than only two interfering trajectories per optical cycle considering the total number of interfering trajectories $M = 2N$, with N being the number of cycles involved in equation (7) [12]. Therefore, the sum over interfering trajectories (equation (7)) can now be decomposed into those associated with two release times within the same cycle and those associated with release times at different cycles [4]. In this sense, the transition probability from the initial state to a final state with momentum $\vec{k}$ (equation (2)) can be written as

$$\frac{\mathrm{d}P}{\mathrm{d}\vec{k}} = 4\Gamma(\vec{k})F(\vec{k})B(k), \qquad (12)$$

where

$$\Gamma(\vec{k}) = \left[\frac{G(t_r^{(1)}, \vec{k}) + G(t_r^{(2)}, \vec{k})}{2}\right]^2, \qquad (13)$$

$$F(\vec{k}) = \cos^2\left(\frac{\Delta S}{2}\right)$$
$$+ \left(\frac{G(t_r^{(1)}, \vec{k}) - G(t_r^{(2)}, \vec{k})}{G(t_r^{(1)}, \vec{k}) + G(t_r^{(2)}, \vec{k})}\right)^2 \sin^2\left(\frac{\Delta S}{2}\right), \qquad (14)$$

and

$$B(k) = \left[\frac{\sin(N\tilde{S}/2)}{\sin(\tilde{S}/2)}\right]^2. \qquad (15)$$

In the calculation of equation (12), we have considered the ionization amplitude $G(t_r^{(\alpha)}, \vec{k})$ to be real. We have regarded that the contribution of the multiple optical cycles in equation (15) is a geometrical sum following the calculations for the one-colour field [4, 10, 11]. For the case of an infinite pulse, i.e., $N \to \infty$, the factor $B(k) \to \sum_n \delta(E - \varepsilon_n)$, with $\varepsilon_n = n\hbar\omega - I_p - U_p$, is in agreement with the conservation of energy for the absorption of n photons. In turn, for a finite number of optical cycles N, the energy peaks have a width (energy difference between the minima besides a principal maxima) $\Delta E = \omega/N$, which fulfills the Heisenberg uncertainty principle $\Delta\varepsilon \tau \sim \hbar$, where τ is the total duration of the pulse ($\tau = N2\pi/\omega$) [4, 10, 11].

Equation (12) indicates that the interference pattern can be factorized in two contributions: (i) the interference stemming from a pair of trajectories within the same optical cycle (*intracycle* interference), governed by the factor $F(\vec{k})$, and (ii) the interference stemming from trajectories released at different optical cycles (*intercycle* interference) resulting in the well-known ATI peaks of the photoelectron spectrum given by $B(k)$ (see [23]). For the case of a laser pulse with a relative phase $\varphi = (j + 1/2)\pi$, the vector potential is symmetric with respect to its maximum (see figure 1(b)), and thus, the electric field is antisymmetric. Therefore, $G(t_r^{(1)}, \vec{k}) = G(t_r^{(2)}, \vec{k})$ and, consequently, the intracycle interference factor takes the form

$$F(\vec{k}) = \cos^2\left(\frac{\Delta S}{2}\right), \qquad (16)$$

J. Phys. B: At. Mol. Opt. Phys. **47** (2014) 204008

D G Arbó

in coincidence with the one-colour case [4, 10, 11], where also $\Gamma(\vec{k}) = |G(t_r^{(1)}, \vec{k})|^2 = |G(t_r^{(2)}, \vec{k})|^2$. For electric fields with a relative phase different from $\varphi = (j + 1/2)\pi$, with integer j, the factor $F(\vec{k})$ is never zero in the classical domain (see equation (14)), making the contrast between maxima and minima poorer than the case for $\varphi = (j + 1/2)\pi$. In other words, the maximum contrast is found for $\varphi = (j + 1/2)\pi$, where $F(\vec{k}) = 0$ at every time that $\Delta S = (2l + 1)\pi$, with integer l. $B(k)$ in equation (12) may be viewed as a diffraction grating in the time domain consisting of N slits and $F(\vec{k})$ as the diffraction factor for each slit consisting of two interfering paths. The intracycle interference arises from the superposition of pairs of classical trajectories separated by a time slit $\Delta t = t_r^{(j,1)} - t_r^{(j,2)}$ of the order of less than half a period of the laser pulse, i.e., $\Delta t < \pi/\omega$. It is important to mention that while for a one-colour pulse, the maximum ionization takes place near threshold (zero final momentum) [4, 10, 11], this is not the general case for two-colour pulses as can be observed in figure 1(b) for $\varphi = \pi/2$. In this case, the maxima of the electric field do not match the zeroes of the vector potential, contrarily to the one-colour case.

3. Results

We have confined our study to ionization of a hydrogen atom initially in its ground state interacting with the two-colour laser field of equation (11), cf figure 1. Calculations within the semiclassical SMM will be compared to the time-dependent continuum distorted wave SFA to determine the level of accuracy of the semiclassical model. More importantly, results within the SFA will be directly compared to results of the CVA in order to determine the effect of the atomic potential of the remaining core on the dynamics of the ejected electron and the ensuing electron distribution. The final verification of the mentioned approximations (SMM, SFA and CVA) will be performed through their comparison with the *ab initio* results by solving numerically the TDSE of equation (1) with no approximations [39].

In the calculation of the electron yield within the SMM, we have used equation (7) and the semiclassical expression for the ionization amplitude $G(t, \vec{k}) = \frac{\pi}{2\sqrt{\tilde{I}_p}|F(t)|} \exp\left[-\frac{(2\tilde{I}_p)^{3/2}}{3|F(t)|}\right]$, where only the flat top region of the pulse was considered, neglecting the adiabatic switch on and switch off. A similar expression for $G(t, \vec{k})$ has been derived from the semiclassical ADK theory [40, 41] and variations of it have been extensively used in the literature (for example, in [35]).

In order to calculate the electron yield within the SFA, CVA and TDSE, we must consider a finite pulse that includes an envelope function $f(t)$ with an appropriate ramp on and off. For the pulse of equation (11), we use an N-cycle flat-top pulse with m-cycle ramp-on and -off,

$$f(t) = F_0 \begin{cases} \sin^2\left(\frac{\omega}{4m}t\right) & \text{if} & 0 \leqslant t < \frac{2m\pi}{\omega} \\ 1 & \text{if} & \frac{2m\pi}{\omega} \leqslant t < \tau - \frac{2m\pi}{\omega} \\ \sin^2\left(\frac{\omega}{4m}(\tau - t)\right) & \text{if} & \tau - \frac{2m\pi}{\omega} \leqslant t \leqslant \tau, \end{cases} \quad (17)$$

where we have chosen $m = 2$ in our calculations and the total pulse duration is equal to a multiple of the laser period, i.e.,

$\tau = n2\pi/\omega$, with $n = 8$ (see figure 1). In this case, the vector potential in the flat top region of the pulse is given by

$$\vec{A}(t) = -\frac{F_0}{\omega}\left[\sin(\omega t) + \frac{1}{2}\sin(2\omega t + \varphi)\right]\hat{z}, \quad (18)$$

and consequently, the ionization times in this region (calculated from either equation (10) or equation (9)) will be the same as for the pulse with adiabatic switch on and off. The envelope function introduced in equation (17) assures not only a smooth switch-on and -off, but also the independence of the intracycle interferences pattern from the pulse duration.

The forward–backward asymmetry of the electron yield can be quantified by the asymmetry coefficient defined as

$$A = \frac{P_{\text{ion}}(+) - P_{\text{ion}}(-)}{P_{\text{ion}}(+) + P_{\text{ion}}(-)}, \quad (19)$$

where $P_{\text{ion}}(\pm)$ is the total electron ejection probabilities in the forward ($k_z > 0$) / backward ($k_z < 0$) direction. When considering a two-colour pulse with $\varphi = 0$ within the SMM or SFA, the asymmetry coefficient $A^{\text{SMM}} = A^{\text{SFA}} = 0$, in agreement with equation (5). We will see that the effect of the Coulomb potential breaks this forward-backward symmetry.

3.1. Photoelectron spectrum

Within the SMM and making use of equations (2) and (7) we have calculated the photoelectron spectrum $\frac{dP}{dE} = 2\pi \int_{\cos\theta_{\text{max}}}^{\cos\theta_{\text{min}}} d(\cos\theta) \sqrt{2E} \left|T_{if}\right|^2$, into a cone of $10°$ along the polarization axis in both forward ($\theta_{\text{min}} = 0$ and $\theta_{\text{max}} = 10°$) and backward ($\theta_{\text{min}} = 170°$ and $\theta_{\text{max}} = 180°$) directions. The two-colour laser pulse of equation (11) has duration of four optical cycles for a flat top field with parameters $F_0 = 0.0533$ and fundamental frequency $\omega = 0.057$. In figure 2(a), we show the photoelectron distribution for relative phase $\varphi = 0$ together with the intracycle interference pattern using equation (12) setting the intercycle factor $B(k)$ to unity. We observe that the photoelectron spectrum consists in a series of multiphoton peaks that are modulated by the intracycle interference pattern corresponding to the contribution of only one optical cycle. From the comparison of the complete photoelectron spectrum and the intracycle envelope, we can directly observe that the intercycle pattern $B(k)$ is responsible for the multiphoton peaks, as equation (15) predicts. The SMM photoelectron spectrum is restricted to the classical region $E < E_{cl} = 2.7U_p \simeq 0.74$.

We have also calculated the photoelectron spectrum within the SFA, which is observed in figure 2(b). We can see that the energy distributions spread beyond the classical boundary E_{cl} highlighting its quantum nature. It is worth mentioning that the SFA photoelectron spectrum of figure 2(b) exhibits modulations similar to the SMM result of figure 1(a), but the position of maxima and minima are not the same. This is a consequence of approximating the ionization times with real values in SMM (equation (10)), instead of complex ionization times as equation (9) indicates. Nonetheless, this lack of accuracy does not undermine the concept of splitting of the intra- and intercycle interference shown in equation (12). Both SMM and SFA photoelectron spectra are forward–backward symmetric for $\varphi = 0$ since the effect of the Coulomb
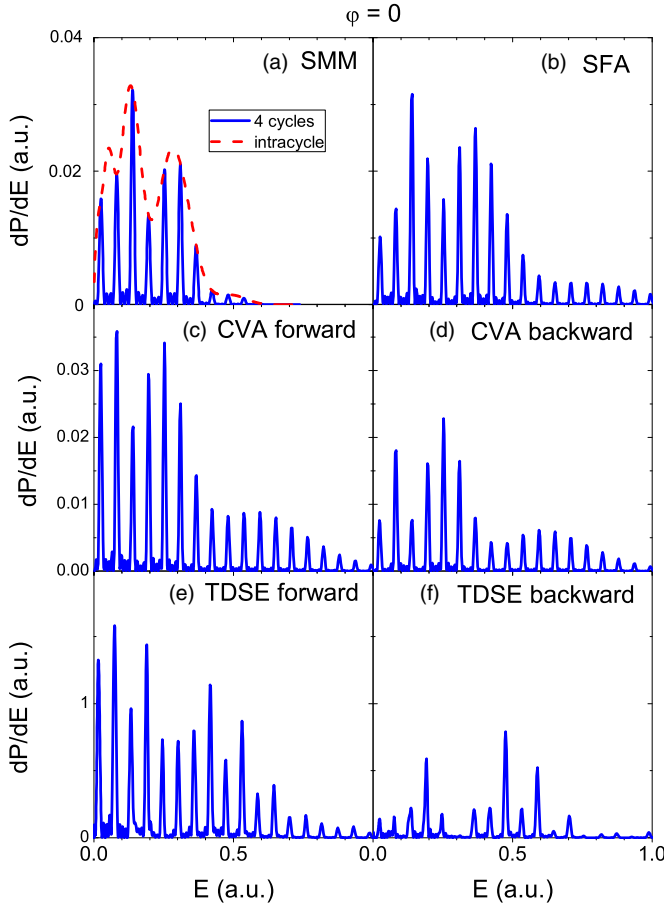
J. Phys. B: At. Mol. Opt. Phys. **47** (2014) 204008

D G Arbó

Figure 2. Photoelectron distribution in a cone of 10° along the polarization axis for the two-colour pulse with amplitude $F_0 = 0.0533$, frequency $\omega = 0.057$ and relative phase $\varphi = 0$. (a) SMM intracycle envelope and four-cycle forward or backward contribution. (b) SFA forward or backward distribution. (c) CVA forward. (d) CVA backward. (e) TDSE forward and (f) TDSE backward. In (a), the spectrum was multiplied by 15 and the intracycle distribution by 240 for a direct comparison with (b). In (b)–(f), the pulse duration is eight optical cycles with a two-cycle ramp on, two-cycle ramp off and four-cycle flat top central region (see figure 1).

Figure 3. Photoelectron distribution in a cone of 10° along the polarization axis for the two-colour pulse with amplitude $F_0 = 0.0533$, frequency $\omega = 0.057$, and relative phase $\varphi = \pi/2$. (a) forward and (b) backward SMM intracycle envelopes and four-cycle contributions. (c) SFA forward and (d) backward distributions. (e) CVA forward and (f) backward distributions. (g) TDSE forward and (h) backward distributions. In (a) and (b), the SMM calculations comprise the four-cycle flat-top region of the pulse. In (b)–(f), the pulse duration is eight optical cycles with a two-cycle ramp on, two-cycle ramp off and four-cycle flat top central region (see figure 1).

potential of the remaining core after ionization on the ejected electron is disregarded in these approaches.

In order to investigate the effect of the Coulomb potential, we calculate the CVA photoelectron spectrum into a cone of 10° in both forward and backward directions. By comparing figures 2(c) and (d), we observe that the Coulomb potential breaks the forward–backward symmetry. The emission is higher in the forward direction than in the backward direction, resulting in an asymmetry factor $A^{\mathrm{CVA}} = 0.3$, which is only caused by the effect of the Coulomb potential on direct electrons. On the contrary, the multiphoton (intercycle) peaks are unaffected by the core potential since they are exclusively determined by factor $B(k)$ through the energy conservation, i.e., $\varepsilon_n = n\hbar\omega - I_p - U_p$. The intracycle envelope can be observed in both directions. If we compare the CVA photoelectron spectrum of figure 2(c) with the SFA of figure 2(b), we observe that the intracycle envelope has shifted towards the threshold. TDSE results show characteristics similar to the CVA outcome with a higher preponderance of
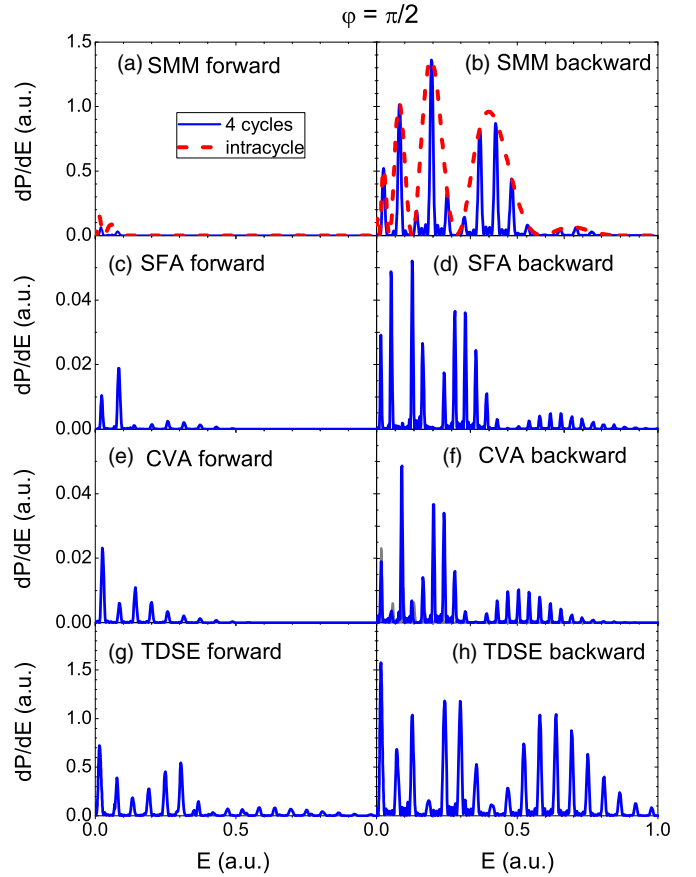
emission in the forward direction, which is evidenced by the asymmetry factor $A^{\mathrm{TDSE}} = 0.51$. Positions of maxima and minima of the envelope do not coincide with the CVA since TDSE calculations account for some other physical processes not considered in CVA, like depletion of the ground state and electron rescattering by the atomic core, which also blurs the visibility of the intracycle pattern.

In figure 3, we show the photoelectron spectra in a cone of 10° along the polarization axis in the forward (left column) and backward (right column) directions for the same electric field of figure 2 but with $\varphi = \pi/2$. We can observe that the electron is mainly ejected in the backward direction. In the first row, we show the SMM predictions together with the intracycle interference pattern. According to the SMM, the energy distribution in the forward direction is restricted to values $E < k_{\mathrm{max}}^2/2 = (9/32)F_0^2/\omega^2 \simeq 0.25$ in figure 3(a) (almost not visible), whereas it is restricted to $E < k_{\mathrm{min}}^2/2 = (9/8)F_0^2/\omega^2 \simeq 0.98$ in the backward direction in figure 3(b). We observe that the forward–backward asymmetry is so important that the emission in the forward

direction (figure 3(a)) is almost negligible compared to the one in the backward direction (figure 3(b)). In this sense, the asymmetry coefficient is $A^{\text{SFA}} = -0.97$. All different spectra in the right column corresponding to the backward direction calculated within the different methods clearly show multiphoton peaks modulated by the intracycle interference pattern. The intracycle envelope shows a sharp contrast, which means, that the intracycle envelope minima are practically zero, in opposition to the case of relative phase $\varphi = 0$ of figure 2, where the interference modulations are less visible since their intracycle minima are considerably different from zero. As discussed for the case of zero relative phase, the SFA intracycle envelope spectra shows a shift with respect to the SMM one because the SMM approximation of equation (10) for the ionization times is not accurate enough. CVA spectrum in the backward direction in figure 3(f) shows a shift of the intracycle interference pattern towards the threshold due to the effect of the Coulomb potential of the residual core. The drop of the asymmetry coefficient to $A^{\text{CVA}} = -0.66$ within the CVA, with respect to $A^{\text{SFA}} = -0.80$, indicates that the effect of the Coulomb potential diminishes the forward–backward asymmetry for $\varphi = \pi/2$. In figure 3(h), we can see that the TDSE spectrum displays an intracycle interference pattern with almost perfect contrast. The position of the maxima and minima of the intracycle interference pattern is similar to the approximations considered (SMM, SFA and CVA) but does not coincide exactly due to depletion of the ground state and rescattering processes, which are considered in TDSE calculations but not in CVA. They are also responsible for the lower forward–backward asymmetry $A^{\text{TDSE}} \simeq -0.58$. In order to have an idea about the importance of the depletion, the total ionization probability for $\varphi = \pi/2$ calculated from figure 3 is about 66%, which evidences a high depletion.

By comparing the SFA and CVA, we can probe directly the effect of the Coulomb phase shift on the interference pattern. When the nuclear charge Z_T is varied in the final-state Coulomb distortion factor of equation (6), the Coulomb phase can be arbitrarily varied between zero and its full value affecting neither the initial-state wave function nor the binding energy. We calculate the photoelectron spectrum into a cone of $10°$ in the backward direction for a laser field of the same parameters used in previous figures for $\varphi = \pi/2$. In figure 4, we observe a monotonic shift of the intracycle envelope $F(k)$ as the strength of the Coulomb potential parametrized by the nuclear charge increases from $Z_T = 0$ (SFA) in figure 4(a) at the top, to $Z_T = 1$ (CVA) in figure 4(e) at the bottom, clearly illustrating the effect of the Coulomb tail on the form factor $F(k)$. In particular, the SFA envelope maxima at $E \simeq 0.95$ and 0.45 move to the CVA maximum at $E \simeq 0.75$ and 0.3, respectively. On the other hand, no significant changes of the multiphoton positions described by $B(k)$ are observed. The monotonic shift caused by the effect of the long-range behaviour of the Coulomb potential has also been observed for one-colour fields [4].

3.2. Doubly differential momentum distribution

In order to provide a complete picture of the emitted electron distribution, we need a two-dimensional description
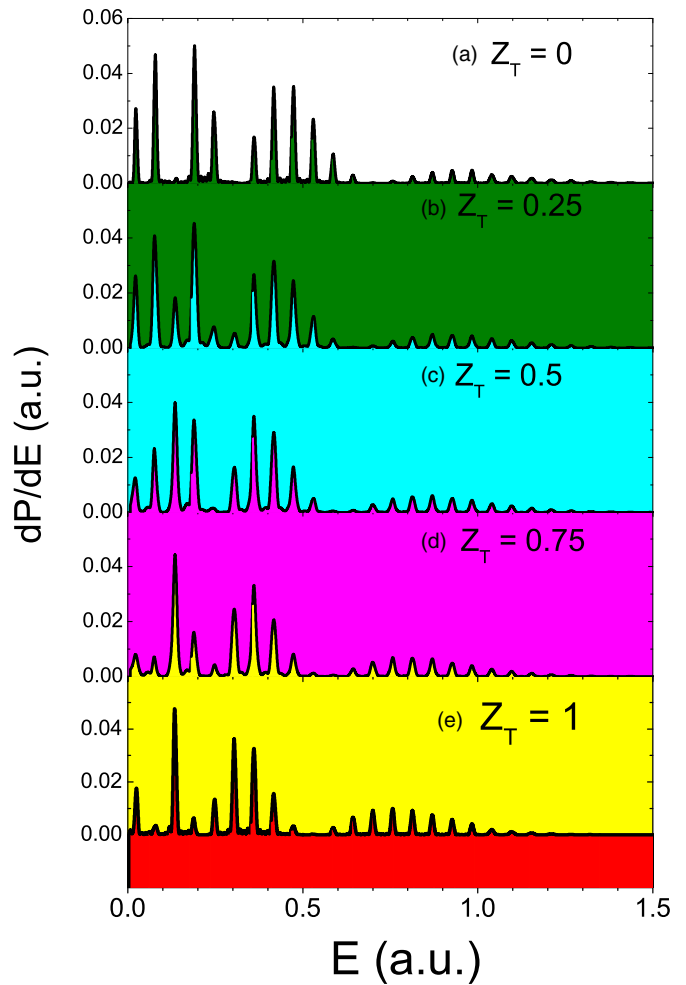

Figure 4. CVA photoelectron spectra in a cone of $10°$ in the backward direction for different values of the nuclear charge $Z_T = 0, 0.25, 0.5, 0.75$ and 1, from the top to the bottom calculated for the eight-cycle pulse described in figure 1. The carrier frequency is $\omega = 0.057$, the field amplitude is $F_0 = 0.0533$ and the relative phase is $\varphi = \pi/2$.

of the electron dynamics since the three-dimensional photoionization problem has cylindrical symmetry around the polarization axis. For that reason, we calculate the doubly differential momentum distributions $\frac{\mathrm{d}^2 P}{\mathrm{d}k_z \mathrm{d}k_\perp} = 2\pi \left| T_{if} \right|^2$, as a function of the longitudinal momentum k_z and the transversal momentum $k_\perp$—the momentum in any direction perpendicular to the polarization axis $\hat{z}$, i.e., $k_\perp = k_x$ or k_y. Figure 5 shows distributions for two-colour electric fields with the same parameters of previous figures with $\varphi = 0$ and $\varphi = \pi/2$ on the left and right columns, respectively. The lower halves of figures 5(a) and (b) show the SMM results for the two-dimensional momentum distribution corresponding to a four-cycle pulse calculated through equation (3). The upper halves exhibit the intracycle pattern by setting the intercycle factor $B(k) = 1$ in equation (12). The intracycle pattern in upper half of figure 5(b) for $\varphi = \pi/2$ clearly modulates the intercycle rings shown in the lower panel of figure 5(b). The SMM longitudinal momentum is symmetrically constrained to $|k_z| < (3\sqrt{3}/2)F_0/\omega \simeq 1.21$ for $\varphi = 0$. Besides, figure 5(b)
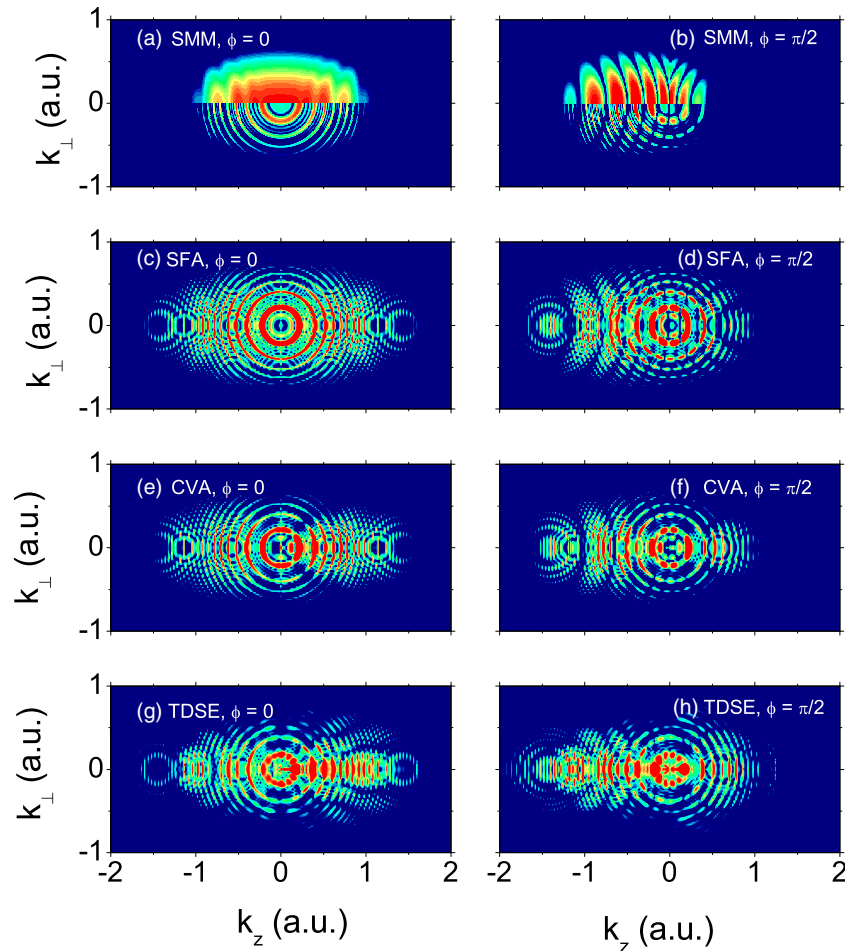
Figure 5. Doubly differential momentum distribution. First column (a), (c), (e) and (g) for $\varphi = 0$ and second column (b), (d), (f) and (h) for $\varphi = \pi/2$. First row (a) and (b) shows the SMM intracycle pattern in the upper halves, whereas the lower halves correspond to the SMM four-cycle contributions. Second row (c) and (d) shows the SFA distributions. Third row (e) and (f) show the CVA distributions. Fourth row (g) and (h) shows the TDSE distributions. The laser parameters are $F_0 = 0.0533$ and $\omega = 0.057$. In (a) and (b), the SMM calculations comprise the four-cycle flat-top region of the pulse. In (c)–(h), the pulse duration is eight-optical cycles with a two-cycle ramp on, two-cycle ramp off and four-cycle flat top central region (see figure 1).

shows the asymmetric SMM longitudinal momentum, which is constrained to $k_{min} < k_z < k_{max}$, where $k_{min} = -(3/2)F_0/\omega \simeq -1.4$ and $k_{max} = (3/4)F_0/\omega \simeq 0.7$. We observe that for the case of $\varphi = 0$ in figures 5(a) and (c), the distributions are symmetric with respect to the line $k_z = 0$ in agreement with equation (5), i.e., $A^{SMM} = A^{SFA} = 0$. This is not the case for $\varphi = \pi/2$ in figures 4(b) and (d), where the 'centre of mass' of the distribution is shifted backwards as recently observed in experiments in helium ionization [1]. Intracycle interference fringes with poor contrast are observed for $\varphi = 0$ in figure 5(a). Quantum calculations (SFA, CVA and TDSE) results in longer distributions beyond the classical boundaries of longitudinal momenta. CVA distributions in figures 4(e) and (f) are slightly narrower (in transversal $k_\perp$ direction) than SFA distributions in figures 4(c) and (d) due to Coulomb focusing. The effect of the Coulomb potential on direct electrons is the reason for the asymmetry of the CVA distribution for $\varphi = 0$ in figure 5(e). This asymmetry is more marked in the TDSE yield in figure 5(g), where radial stripes are observed in the forward direction, probably a signature of rescattering processes [42–44]. When

we compare CVA and SFA distributions for $\varphi = \pi/2$, we observe that the CVA intracycle fringes in figure 5(f) are a little shifted towards the origin with respect to the SFA ones in figure 5(d), the same effect exhibited in figure 4 for the photoelectron spectrum in the backward direction for $\varphi = \pi/2$. TDSE distribution in figure 5(h) displays similar interference patterns to CVA, SFA and SMM, something that ensures the approximating methods employed. Furthermore, TDSE results for hydrogen in figure 5(h) are very similar to figure 2(f) in [1]. Despite the authors of [1] do not analyse the intracycle interference pattern, this can be clearly observed in their simulations and experiments (see figure 2(d) of [1] and also [2]).

3.3. Longitudinal momentum distribution

We have also calculated the longitudinal momentum distribution dP/dk_z integrating the doubly differential momentum distributions of figure 5 over the transversal
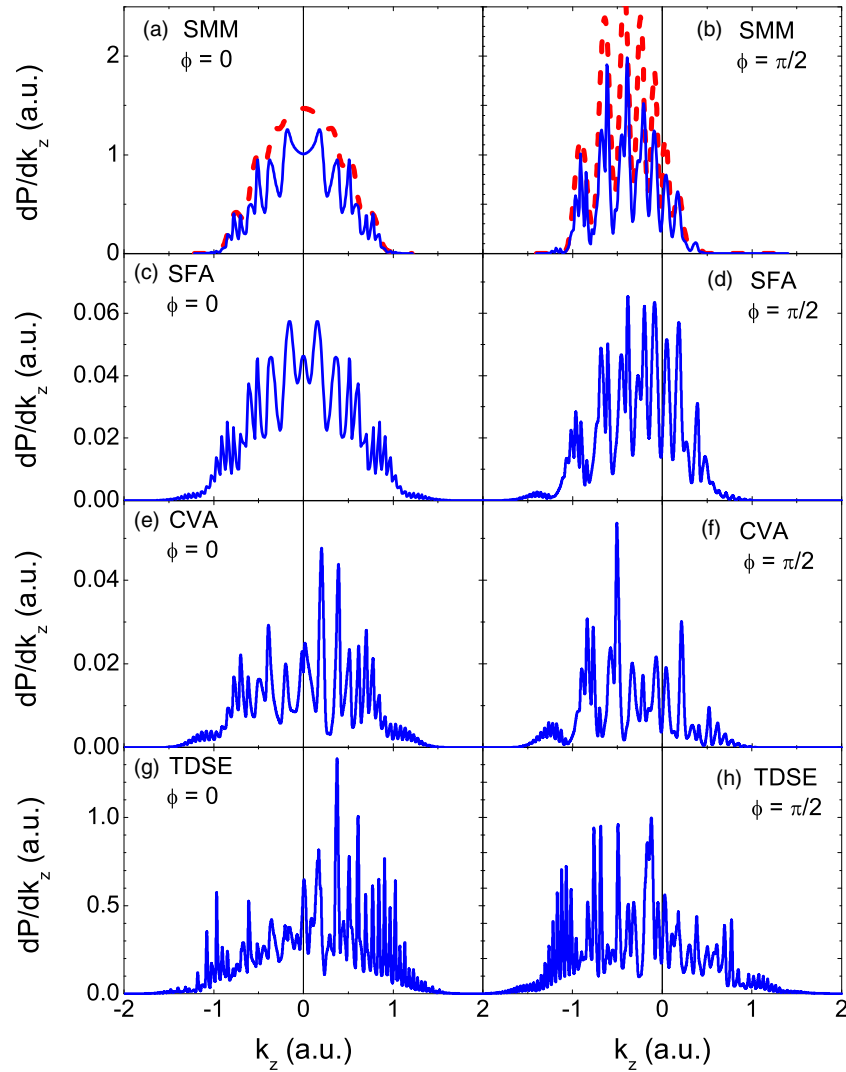
Figure 6. Longitudinal momentum distribution integrated over the transversal momentum. First column (a), (c), (e) and (g) for $\varphi = 0$ and second column (b), (d), (f), and (h) for $\varphi = \pi/2$. First row (a) and (b) shows the SMM intracycle pattern together the four-cycle contribution. Second row (c) and (d) shows the SFA distributions. Third row (e) and (f) show the CVA distributions. Fourth row (g) and (h) shows the TDSE distributions. In (a) and (b), the SMM calculations comprise the four-cycle flat-top region of the pulse. The laser parameters are $F_0 = 0.0533$ and $\omega = 0.057$. In (c)–(h) the pulse duration is eight optical cycles with a two-cycle ramp on, two-cycle ramp off and four-cycle flat top central region (see figure 1).

momentum, i.e., $\frac{dP}{dk_z} = 2\pi \int_0^\infty dk_\rho \; k_\rho \left| T_{if} \right|^2$. We show the results in figure 6: the left column exhibits results for $\varphi = 0$ and the right column does it for $\varphi = \pi/2$. We observe that in figures 6(a) and (c), the SMM and SFA distribution for $\varphi = 0$ are symmetric as expected from equation (5). The corresponding distributions for $\varphi = \pi/2$ are displaced towards the negative values of k_z. From figure 6(e), we see that for $\varphi = 0$ the Coulomb potential tilts a little the momentum distribution towards the positive values of k_z with respect to the SFA distribution in figure 6(c). These results corroborate recent studies using the strong-field classical trajectory model, which corresponds to the quasiclassical limit of the SMM [1], in which path interferences are neglected. By considering path interferences, we can see, on one hand, the intracycle envelope for high longitudinal momenta where the intercycle peak separation is small compared to the intracycle oscillations. On the other hand, since near the threshold, the intercycle peak separation competes with the intracycle oscillations, we cannot

distinguish the intracycle pattern from the whole momentum distribution. TDSE results in figures 5(g) and (h) reproduce quite well the CVA results, however, it fades out at slightly higher values of longitudinal momentum (in absolute values) compared to the CVA distributions. Electron rescattering by the residual core may probably be the reason of this. We want to stress that in figure 6(h) for $\varphi = \pi/2$, the TDSE intracycle interference pattern can be clearly observed as two envelope maxima at $k_z \simeq -1.1$ and -0.7. Corresponding intracycle oscillations for $\varphi = 0$ in figure 6(g) situated at $k_z \simeq -1$ and -0.6 are also observed, even though not as clearly as for $\varphi = \pi/2$.

4. Conclusions

In this article, we have presented a study about interference effects resulting from the interaction of an isolated atom with intense two-colour laser pulses, where the second frequency

doubles the fundamental. We have put special emphasis on the action of the Coulomb potential of the ionic core on the electron yield. We followed a simple semiclassical model based on the SMM [12] which identifies the interplay between the intra- and intercycle interferences of electron trajectories in multicycle two-colour laser photoionization. However, the SMM is not accurate enough when it comes to quantifying the intracycle pattern that extends beyond the classical domain. Therefore, time-dependent distorted-wave approximations SFA and CVA were presented. We have explored the effect of the Coulomb potential on the electron yield, especially on the interference pattern by comparing the CVA and SFA result. We show that the Coulomb potential affects the interference pattern in the whole domain by shifting the intracycle modulations towards the threshold in the photoelectron spectrum. On the contrary, the intercycle interference pattern recognized as multiphtoton peaks in the photoelectron spectrum is invariant to the presence of the Coulomb potential since it is only consequence of energy conservation in the photon absorption process. This result, already known for the case of atomic ionization by one-colour laser fields [10], has been extended to the case of sculpted laser fields with two commensurate frequencies ($\omega - 2\omega$) stressing the coherent control provided by the relative phase φ, which works as a knob to manipulate the intracycle interference.

Approximating methods SFA and CVA were tested against the solutions of the TDSE, which show clear evidence of intracycle interferences. Coherent superposition of electron wave packets released within the same sculpted optical cycle are clearly observed in TDSE calculations involving laser pulses with relative phase between the two colours $\varphi = \pi/2$. The theory explains attosecond strong-field electron wavepacket interferometry experiments with sub-ten-attosecond precision [2]. The dependence of the intracycle modulations on the long-range atomic Coulomb potential might open the possibility of imaging the core potential in the experimentally easy to obtain direct electron yield. In view of TDSE doubly differential momentum distributions, novel structures appear which are worth studying in future investigations.

Acknowledgments

References

[1] Xie X *et al* 2013 *New J. Phys.* **15** 043050
[2] Xie X *et al* 2012 *Phys. Rev. Lett.* **108** 193004
[3] Corkum P B, Burnett N H and Ivanov M Y 1994 *Opt. Lett.* **19** 1870
[4] Arbó D G, Ishikawa K L, Schiessl K, Persson E and Burgdörfer J 2010 *Phys. Rev.* A **81** 021403
[5] Lindner F, Schätzel M G, Walther H, Baltuška A, Goulielmakis E, Krausz F, Milošević D B, Bauer D, Becker W and Paulus G G 2005 *Phys. Rev. Lett.* **95** 040401
[6] Gopal R *et al* 2009 *Phys. Rev. Lett.* **103** 053001
[7] Arbó D G, Persson E and Burgdörfer J 2006 *Phys. Rev.* A **74** 063407
[8] Bergues B, Ansari Z, Hanstorp D and Kiyan I Y 2007 *Phys. Rev.* A **75** 063415
[9] Bivona S, Bonanno G, Burlon R, Gurrera D and Leone C 2008 *Phys. Rev.* A **77** 051404
Bivona S, Bonanno G, Burlon R and Leone C 2009 *Phys. Rev.* A **79** 035403
[10] Arbó D G, Ishikawa K L, Schiessl K, Persson E and Burgdörfer J 2010 *Phys. Rev.* A **82** 043426
[11] Arbó D G, Ishikawa K L, Schiessl K and Burgdörfer J 2012 *Nucl. Instrum. Methods* B **279** 24
[12] Arbó D G, Nagele S, Tong X-M, Xie X, Kitzler M and Burgdörfer J 2014 *Phys. Rev.* A **89** 043419
[13] Ehlotzky F 2001 *Phys. Rep.* **345** 175
[14] Schumacher D W, Weihe F, Muller H G and Bucksbaum P H 1994 *Phys. Rev. Lett.* **73** 1344
[15] Muller H G, Bucksbaum P H, Schumacher D W and Zavriyev A 1990 *J. Phys. B: At. Mol. Opt. Phys.* **23** 2761
[16] Ohmura H, Nakanaga T and Tachiya M 2004 *Phys. Rev. Lett.* **92** 113002
[17] Fifrig M, Cionga A and Ehlotzky F 2003 *Eur. Phys. J.* D **23** 333
[18] Cionga A, Fifrig M and Ehlotzky F 2003 *J. Mod. Opt.* **50** 615
[19] De S *et al* 2009 *Phys. Rev. Lett.* **103** 153002
[20] Keldysh V 1964 *Zh. Eksp. Theor. Fiz.* **47** 1945
Keldysh V 1965 *Sov. Phys.—JETP* **20** 1307
[21] Faisal F H M 1973 *J. Phys. B: At. Mol. Phys.* **6** L89
[22] Reiss H 1980 *Phys. Rev.* A **22** 1786
[23] Faisal F H M and Schlegel G 2005 *J. Phys. B: At. Mol. Opt. Phys.* **38** L223
[24] Dewangan D P and Eichler J 1997 *Phys. Rep.* **247** 59
[25] Arbó D G, Miraglia J E, Gravielle M S, Schiessl K, Persson E and Burgdörfer J 2008 *Phys. Rev.* A **77** 013401
[26] Volkov D M 1935 *Z. Phys.* **94** 250
[27] Arbó D G, Yoshida S, Persson E, Dimitriou K I and Burgdörfer J 2006 *Phys. Rev. Lett.* **96** 143003
Arbó D G, Dimitriou K I, Persson E and Burgdörfer J 2008 *Phys. Rev.* A **78** 013406
[28] Jain M and Tzoar N 1978 *Phys. Rev.* A **18** 538
[29] Basile A, Trombetta F, Ferrante G, Burlon R and Leone C 1988 *Phys. Rev.* A **37** 1050
[30] Milosevic D V and Ehlotzky F 1998 *Phys. Rev.* A **58** 3124
[31] Kaminski J Z, Jaron A and Ehlotzky F 1996 *Phys. Rev.* A **53** 1756
[32] Figueira de Morrison Faria C, Schomerus H and Becker W 2002 *Phys. Rev.* A **66** 043413
[33] Macri P A, Miraglia J E and Gravielle M S 2003 *J. Opt. Soc. Am.* B **20** 1801
[34] Rodriguez V D, Cormier E and Gayet R 2004 *Phys. Rev.* A **69** 053402
Rodriguez V D, Macri P and Arbó D G 2009 *Nucl. Instrum. Methods* B **267** 334
[35] Chirila C C and Potvliege R M 2005 *Phys. Rev.* A **71** 021402(R)
[36] Lewenstein M, Kulander K C, Schafer K J and Bucksbaum P H 1995 *Phys. Rev.* A **51** 1495
Lewenstein M, Balcou Ph, Ivanov M Yu, L'Huillier A and Corkum P B 1994 *Phys. Rev.* A **49** 2117
[37] Ivanov M, Corkum P B, Zuo T and Bandrauk A 1995 *Phys. Rev. Lett.* **74** 2933
[38] Milošević D B, Hasović E, Odžak S, Busuladžić M, Gazibegović-Busuladžić A and Becker W 2008 *J. Mod. Opt.* **55** 2653
Milošević D B and Becker W 2002 *Phys. Rev.* A **66** 063417
[39] Tong X-M and Chu S I 1997 *Chem. Phys.* **217** 119
Tong X-M and Lin C D 2005 *J. Phys. B: At. Mol. Opt. Phys.* **38** 2593
Arbó D G, Yoshida S, Persson E, Dimitriou K I and Burgdörfer J 2007 *J. Phys.: Conf. Ser.* **88** 012054

[40] Ammosov M V, Delone N B and Krainov V P 1986 *Zh. Eksp. Teor. Fiz.* **91** 2008
　　　Ammosov M V, Delone N B and Krainov V P 1986 *Sov. Phys.—JETP* **64** 1191
[41] Delone N B and Krainov V P 1991 *J. Opt. Soc. Am.* B **8** 1207

[42] Huismans Y *et al* 2011 *Science* **331** 61
[43] Huismans Y *et al* 2012 *Phys. Rev. Lett.* **109** 013002
[44] Marchenko T, Muller H G, Schafer K J and Vrakking M J J 2010 *J. Phys. B: At. Mol. Opt. Phys.* **43** 095601